Multishocked, Three-Dimensional Supersonic Flowfields with Real Gas Effects

P. KUTLER,* W. A. REINHARDT,† AND R. F. WARMING*
NASA Ames Research Center, Moffett Field, Calif.

A computational procedure is presented which is capable of determining the supersonic flowfield surrounding three-dimensional wing-body configurations of a delta-wing space shuttle. The governing equations in conservation-law form are solved by a finite-difference method using a second-order noncentered algorithm between the body and the outermost shock wave, which is treated as a sharp discontinuity. Secondary shocks which form between these boundaries are captured automatically, and the intersection of these shocks with the peripheral shock posed no difficulty. Resulting flowfields about typical blunt nose shuttlelike configurations at angle of attack are presented. The differences between perfect and real gas effects for high Mach number flows are shown.

I. Introduction

THE numerical computation of three-dimensional inviscid, flowfields for either perfect or real gases about supersonic or hypersonic airplanes and re-entry spacecraft such as the space shuttle is of considerable interest to the vehicle designer. The complicated geometry of typical configurations cruising at supersonic velocities or entering the Earth's atmosphere results in an intricate three-dimensional flowfield consisting of multiple shocks, expansion waves, and slip surfaces. The purpose of this paper is to describe a numerical procedure for calculating the details of such flowfields for both perfect and real gases (i.e., gases in local thermodynamic equilibrium) by utilizing a second-order noncentered finite-difference scheme. Aircraft and re-entry spacecraft designed for efficient flight usually have blunt noses and therefore an embedded region of subsonic flow. But aside from this small region, the downstream flowfield is entirely supersonic. Consequently, the governing gasdynamic equations are hyperbolic, and given a starting solution there follows a well-posed initial-value problem.

There are currently at least two numerical approaches for handling the flow discontinuities of a multishocked flowfield. In one (see, e.g., Ref. 1), the bow shock and one other internal shock (either crossflow, canopy, or wing leading edge) are treated as discontinuities across which the Rankine-Hugoniot equations are applied. To date, it has been used successfully in calculating supersonic flows about simplified wing-body configurations. Although it is conceptually possible to treat all shock waves as well as slip surfaces as sharp discontinuities, the method would involve complex logic and would be particularly difficult to set up for automatic computation.

The other numerical procedure, termed a shock capturing technique (see, e.g., Ref. 2), is inherently capable of predicting the location and strength of all shocks without explicit use of any special shock fitting procedures. The equations are cast in conservation-law form, and starting from an initial data plane, integrated numerically downstream using MacCormack's[3] second-order noncentered difference algorithm. Results have been obtained using this procedure for configurations which generate secondary shocks due to the canopy and the wing leading edge. The shocks, however, are spread over several mesh intervals and require a sufficient number of grid points to accurately capture them. The results obtained demonstrate the methods capability for easily treating complex flows.

It would seem plausible that to alleviate the problems encountered while locating and treating all shocks as sharp discontinuities and at the same time to increase the efficiency and accuracy of shock capturing techniques, one should construct a hybrid system that treats certain shocks as sharp and captures others. Such a numerical procedure is presented in this paper.

The outermost shock, i.e., the shock which separates the free-stream from the disturbed region generated by the body in this procedure, is treated as a sharp discontinuity. For example, before the canopy or wing is reached, the outermost shock is that generated by the nose of the vehicle. If the shock generated by the canopy or the wing intersects the bow shock, the resulting coalesced shock then becomes the outermost shock. Hence, there are segments of the outermost shock which could consist of the original nose shock, the canopy shock, and the wing leading edge shock. The resulting flowfield between the body and outermost shock is treated in a shock-capturing fashion[2] and therefore allows for the correct formation of secondary internal shocks.

II. Review of Governing Equations

The fluid dynamic equations in conservation-law form governing steady, inviscid, three-dimensional, compressible flow of a nonheat-conducting gas can be written in cylindrical coordinates (Fig. 1) as follows:

$$\partial\tilde{\mathbf{U}}/\partial z+\partial\tilde{\mathbf{F}}/\partial r+\partial\tilde{\mathbf{G}}/\partial\phi+\tilde{\mathbf{H}}=0 \tag{1}$$

where $\tilde{\mathbf{U}}$, $\tilde{\mathbf{F}}$, $\tilde{\mathbf{G}}$, and $\tilde{\mathbf{H}}$ are four-component vectors defined as

$$\tilde{\mathbf{U}}=\begin{vmatrix}\rho u\\ p+\rho u^2\\ \rho uv\\ \rho uw\end{vmatrix}\qquad \tilde{\mathbf{F}}=\begin{vmatrix}\rho v\\ \rho uv\\ p+\rho v^2\\ \rho vw\end{vmatrix}$$

$$\tilde{\mathbf{G}}=\frac{1}{r}\begin{vmatrix}\rho w\\ \rho uw\\ \rho vw\\ p+\rho w^2\end{vmatrix}\qquad \tilde{\mathbf{H}}=\frac{1}{r}\begin{vmatrix}\rho v\\ \rho uv\\ \rho(v^2-w^2)\\ 2\rho vw\end{vmatrix}$$

Here p and ρ represent dimensional pressure and density and u, v, and w denote velocity components in the coordinate

Presented as AIAA Paper 72-702 at the AIAA 5th Fluid and Plasma Dynamics Conference, Boston, Mass., June 26–28, 1972; submitted July 21, 1972; revision received January 11, 1973.

Index categories: Supersonic and Hypersonic Flow; Reactive Flows; Entry Vehicles and Landers.

* Research Scientist. Member AIAA.

† Research Scientist. Associate Fellow AIAA.

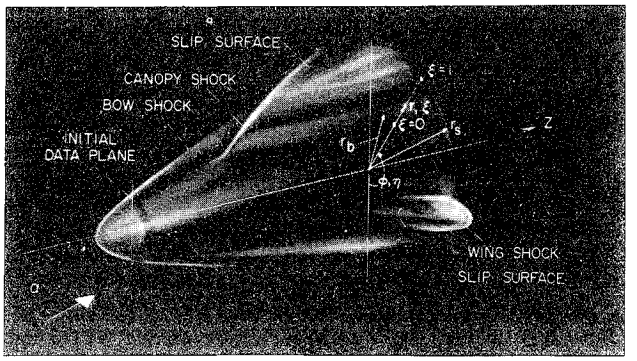

Fig. 1 Description of coordinate system.

directions z, r, and ϕ. The nonlinear system (1) of four equations represents conservation of mass and momentum.

The governing set of equations is made complete by the addition of energy conservation as given by the equation for total enthalpy

$$H_t = h(p,\rho)+q^2/2 = \text{const} \tag{2}$$

where q is the magnitude of the velocity vector and $h(p,\rho)$ is the state equation for static enthalpy. The specific formulation for h depends, in particular, on whether the gas is assumed to be perfect or everywhere in local thermodynamic equilibrium. Explicit representations for h are described later.

The vehicle geometry and the location of the outer or peripheral shock surface as illustrated in Fig. 1 are represented by functions of the form

$$r_b = r_b(z,\phi), \quad r_s = r_s(z,\phi) \tag{3}$$

The function r_b is specified (Sec. III) and r_s is determined during the course of the numerical computation (Sec. V). As is common practice in problems of this type, the distance between the body and peripheral shock is normalized (see Fig. 2a) by a transformation of the radial variable r. This yields a rectangular computational plane whose boundaries consist of the plane of symmetry and the body and shock surfaces as shown in Fig. 2b.

Since the flow variables can vary rapidly in the cross flow plane, an independent variable transformation is performed in the ϕ direction to cluster points in that region of suspected large gradients. The transformation, which is also given below, was introduced by Woods[4] and has been successfully applied by Schiff.[5]

The equations of the independent variable transformations are

$$z = z, \quad \xi(z,r,\phi) = (r-r_b)/(r_s-r_b), \quad \eta(\phi) = \tan^{-1}(\kappa\tan\phi) \tag{4}$$

where κ is a free parameter with the range $0 < \kappa \leqq 1$. The points are clustered about the wing tip region (90° plane) for small values of κ and the spacing approaches uniformity as κ approaches unity.

The change of variable procedure outlined above is applied to each vector of Eq. (1), and the resulting terms are then rearranged in conservation-law form to yield the following equation:

$$\partial\mathbf{U}/\partial z+\partial\mathbf{F}/\partial\xi+\partial\mathbf{G}/\partial\eta+\mathbf{H} = 0 \tag{5}$$

where

$$\mathbf{U} = \tilde{\mathbf{U}}$$

$$\mathbf{F} = \{-[r_{b_z}+\xi(r_{s_z}-r_{b_z})]\tilde{\mathbf{U}}+\tilde{\mathbf{F}}-[r_{b_\phi}+\xi(r_{s_\phi}-r_{b_\phi})]\tilde{\mathbf{G}}\}/(r_s-r_b)$$

$$\mathbf{G} = (\kappa^2\cos^2\eta+\sin^2\eta)\tilde{\mathbf{G}}/\kappa$$

$$\mathbf{H} = \tilde{\mathbf{H}}+[(r_{s_z}-r_{b_z})\tilde{\mathbf{U}}+(r_{s_\phi}-r_{b_\phi})\tilde{\mathbf{G}}]/(r_s-r_b)-(1-\kappa^2)\sin(2\eta)\tilde{\mathbf{G}}/\kappa$$

The finite-difference analogue of Eq. (5) is integrated with respect to the hyperbolic coordinate z to yield values of the conservative variable $\mathbf{U}$. Subsequent to each integration step, the physical flow variables p, ρ, u, v, and w must be decoded from the components u_i of $\mathbf{U}$. This necessitates the solution of five, simultaneous, nonlinear equations consisting of Eq. (2) together with the four elements u_i. The velocity components v and w are easily found and are given by

$$v = u_3/u_1, \quad w = u_4/u_1 \tag{6}$$

If the u_i along with Eqs. (6) are used to eliminate the explicit dependence of p, ρ, v, and w from Eq. (2), one obtains the following implicit expression for the velocity u:

$$E(u) = u^2/2+h[p(u),\rho(u)]-\Gamma/2 = 0 \tag{7}$$

where

$$p(u) = u_2-u_1u, \quad \rho(u) = u_1/u, \quad \text{and} \quad \Gamma = 2H_t-[u_3^2+u_4^2]/u_1^2 \tag{8}$$

The decoding procedure is now reduced to a problem of root finding, i.e., the z-velocity component u that satisfies Eq. (7). Two roots exist; one corresponds to subsonic flow and is discarded since in the results presented u is always supersonic, and the other corresponds to supersonic flow and gives the desired solution. The procedure for solving Eq. (7) depends on whether a perfect or real gas is being considered and consequently on the function $h(p,\rho)$.

For a perfect gas $h(p,\rho)$ is simply related to pressure and density and when combined with Eqs. (7 and 8) yields a quadratic equation that can be solved to find an analytical representation[2] for the supersonic velocity u.

For a real gas no such simple explicit functional relationship exists. The conventional procedure[1,6] for evaluating real gas state relations is to use a combination table lookup and curve-fitting procedure. Such a scheme is adopted here. A particularly rapid Fortran-language computer code called RGAS is available‡ that returns values of static enthalpy h, speed of sound, temperature, and entropy, with either pressure and density or pressure and entropy as independent variables.

To find the roots of Eq. (7) for a real gas, a root finding algorithm is employed. The "successive linear interpolation" scheme described by Dekker[7] was found to be particularly efficient. Slightly more than seven iterations are required, on the average, to find the desired supersonic root for a given U (three iterations is the happenstance absolute minimum).

Three-dimensional numerical integration methods (see, e.g., Refs. 1, 6, and 8) which employ physical rather than conservative dependent variables are generally able to include state relations in a more direct manner since a decoding procedure is not necessary. Only half again more computational time than a perfect gas calculation is required for those codes compared to a factor of about four when conservative variables are employed. However, the ability to capture shocks by use of conservative variables is worth the additional cost.

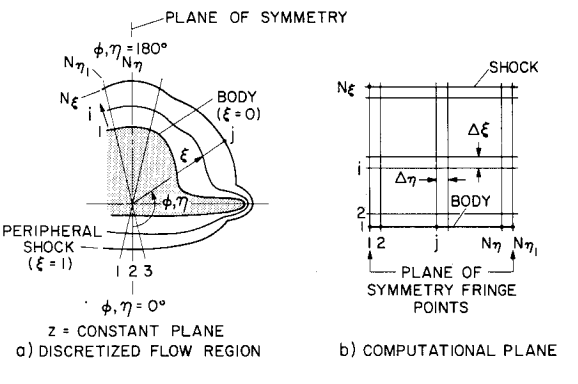

Fig. 2 Mesh description.

‡ This code is available on request from the Computational Fluid Dynamics Branch, NASA Ames Research Center.

SEGMENT	FUNCTION
① - ②	STRAIGHT LINE
② - ③	ELLIPSE
③ - ④	STRAIGHT LINE
④ - ⑤	CUBIC POLYNOMIAL
⑤ - ⑥	STRAIGHT LINE
⑥ - ⑦	ELLIPSE

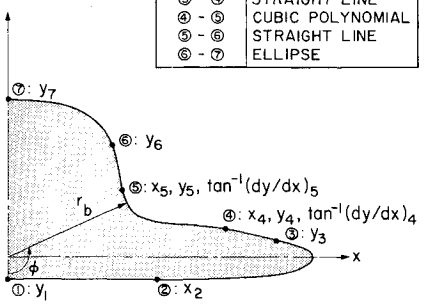

Fig. 3 Typical body cross section.

III. Body Geometry

A more sophisticated body geometry package has been developed than was used in Ref. 2. The simulation of an actual aircraft or spacecraft geometry is done by analytic approximations. The body geometry package that was devised is similar to that of Chu and Powers[9] and is more suitable for shuttlelike configurations than our previous designs.[2] A typical cross section of the body at a given longitudinal coordinate z is composed of the analytic functions illustrated in Fig. 3. These six segments require specification of the eleven geometrical parameters listed in the figure as a function of the longitudinal distance z to completely describe a typical vehicle. Some segments can have zero length.

The longitudinal variation of the eleven geometrical parameters and their derivatives with respect to z are required by the program. We arbitrarily require that the analytic approximation of the body be single valued, continuous, and have continuous first derivatives. To ensure this requirement, discrete values for each of the parameters and their first derivatives are obtained at various stations along the body from working drawings of a particular vehicle or spacecraft configuration (these parameters need not necessarily be defined at the same z coordinates). Then for each of these parameters a cubic polynomial, which is determined so as to maintain the continuity requirements at the end points, is used to describe the variation between the points.

IV. Finite-Difference Scheme

Since only the peripheral shock is treated as a sharp discontinuity and the others are "captured" by the difference algorithm, of prime importance is the selection of the finite-difference scheme to be used to advance the field points, i.e., the points for which $2 \leqq i \leqq N_\xi - 1$ and $2 \leqq j \leqq N_\eta$ in Fig. 2b. It has been found[10] that MacCormack's scheme,[3] which is an accurate predictor-corrector scheme, is the most efficient second-order algorithm to use in a shock-capturing technique.

The algorithm can be written as

$$\mathbf{U}_{i,j}^{(1)} = \mathbf{U}_{i,j}^{n} - \frac{\Delta z}{\Delta \xi}(\mathbf{F}_{i+1,j}^{n} - \mathbf{F}_{i,j}^{n}) - \frac{\Delta z}{\Delta \eta}(\mathbf{G}_{i,j+1}^{n} - \mathbf{G}_{i,j}^{n}) - \Delta z \mathbf{H}_{i,j}^{n} \tag{9a}$$

$$\mathbf{U}_{i,j}^{n+1} = \frac{1}{2}\left\{\mathbf{U}_{i,j}^{n} + \mathbf{U}_{i,j}^{(1)} - \frac{\Delta z}{\Delta \xi}[\mathbf{F}_{i,j}^{(1)} - \mathbf{F}_{i-1,j}^{(1)}] - \frac{\Delta z}{\Delta \eta}[\mathbf{G}_{i,j}^{(1)} - \mathbf{G}_{i,j-1}^{(1)}] - \Delta z \mathbf{H}_{i,j}^{(1)}\right\} \tag{9b}$$

where

$$\mathbf{U}_{i,j}^{n} = \mathbf{U}(n\Delta z, i\Delta\xi, j\Delta\eta)$$
$$\mathbf{F}_{i,j}^{n} = \mathbf{F}(\mathbf{U}_{i,j}^{n}, n\Delta z, i\Delta\xi, j\Delta\eta)$$
$$\mathbf{F}_{i,j}^{(1)} = \mathbf{F}(\mathbf{U}_{i,j}^{(1)}, (n+1)\Delta z, i\Delta\xi, j\Delta\eta)$$

At the body ($i = 1, 2 \leqq j \leqq N_\eta$) Abbett's[11] scheme is used to satisfy the surface tangency condition as is discussed in Sec. V. It relies on information provided by the finite-difference scheme. The numerical algorithm used for the field points, however, cannot be used on the surface since it requires points on either side of the point being advanced and thus data at a set of points that would lie within the body. Consequently, a special second-order accurate algorithm was constructed which requires data only on or outside the body. This scheme uses the predictor step of MacCormack's method,[10,3] Eq. (9a), followed by the corrector step given by

$$\mathbf{U}_{i,j}^{n+1} = \frac{1}{2}\left[\mathbf{U}_{i,j}^{n} + \mathbf{U}_{i,j}^{(1)} - \frac{\Delta z}{\Delta \xi}(\mathbf{F}_{i+1,j}^{(1)} - \mathbf{F}_{i,j}^{(1)}) - \frac{\Delta z}{\Delta \eta}(\mathbf{G}_{i,j}^{(1)} - \mathbf{G}_{i,j-1}^{(1)}) - \Delta z \mathbf{H}_{i,j}^{(1)} + \frac{\Delta z}{\Delta \xi}(\mathbf{F}_{i+2,j}^{n} - 2\mathbf{F}_{i+1,j}^{n} + \mathbf{F}_{i,j}^{n})\right] \tag{10}$$

where $i = 1$. After MacCormack's predictor and Eq. (10) have been used to advance the data at the body, then Abbett's scheme is used as a final corrector.

At the shock wave, a predictor-corrector sequence is again used and requires data at the shock and one point below it. The algorithm is as follows:

$$\mathbf{U}_{i,j}^{(1)} = \mathbf{U}_{i,j}^{n} - \frac{\Delta z}{\Delta \xi}(\mathbf{F}_{i,j}^{n} - \mathbf{F}_{i-1,j}^{n}) - \frac{\Delta z}{\Delta \eta}(\mathbf{G}_{i,j+1}^{n} - \mathbf{G}_{i,j}^{n}) - \Delta z \mathbf{H}_{i,j}^{n} \tag{11a}$$

$$\mathbf{U}_{i,j}^{n+1} = \frac{1}{2}\left[\mathbf{U}_{i,j}^{n} + \mathbf{U}_{i,j}^{(1)} - \frac{\Delta z}{\Delta \xi}(\mathbf{F}_{i,j}^{(1)} - \mathbf{F}_{i-1,j}^{(1)}) - \frac{\Delta z}{\Delta \eta}(\mathbf{G}_{i,j}^{(1)} - \mathbf{G}_{i,j-1}^{(1)}) - \Delta z \mathbf{H}_{i,j}^{(1)}\right] \tag{11b}$$

where $i = N_\xi$. Equations (11a) and (11b) are used in conjunction with the Rankine-Hugoniot relations, as described in Sec. V, to determine the peripheral shock slope.

The integration stepsize is based on the analysis presented in Ref. 2, in which formulas for the projections of the slopes of the characteristics in the $z-\xi$ and $z-\phi$ planes are given and, with a slight modification due to the clustering transformation of ϕ, can be used to determine the maximum possible stepsize.

V. Boundary Conditions

In this section the boundary condition schemes applied at the body and shock surfaces are discussed briefly. At the body the surface tangency condition

$$\mathbf{q} \cdot \mathbf{n}_b = 0 \tag{12}$$

is imposed where $\mathbf{q}$ is the velocity vector

$$\mathbf{q} = u\mathbf{i}_z + v\mathbf{i}_r + w\mathbf{i}_\phi \tag{13}$$

and $\mathbf{n}_b$ is the outward unit normal to the body. The second-order predictor-corrector scheme, MacCormack's predictor and Eq. (10), is first applied at the body to yield the conservative variables. These variables are then decoded [see discussion following Eq. (6)] to obtain $\bar{p}_{1,j}^{n+1}$, $\bar{\rho}_{1,j}^{n+1}$, $\bar{u}_{1,j}^{n+1}$, $\bar{v}_{1,j}^{n+1}$, and $\bar{w}_{1,j}^{n+1}$ at z^{n+1}. In general the resulting velocity vector $\bar{\mathbf{q}}_{1,j}^{n+1}$ based on the predicted velocity components will not satisfy the surface tangency condition Eq. (12) and, in fact, will be rotated out of the surface tangent plane by a small angle $\Delta\theta$. In applying Abbett's method[11] this angle can be determined from the following equation:

$$\Delta\theta = \sin^{-1}(\bar{\mathbf{q}}_{1,j}^{n+1} \cdot \mathbf{n}_b / \bar{q}_{1,j}^{n+1}) \tag{14}$$

where $\bar{q}_{1,j}^{n+1}$ is defined to be the magnitude of $\bar{\mathbf{q}}_{1,j}^{n+1}$ and the outward unit normal $\mathbf{n}_b$ to the body can be calculated from (see Ref. 2)

$$\mathbf{n}_b = \frac{\nabla f_b}{|\nabla f_b|} = \frac{-r_{b_z}\mathbf{i}_z + \mathbf{i}_r - (r_{b_\phi}/r_b)\mathbf{i}_\phi}{[r_{b_z}^2 + 1 + (r_{b_\phi}/r_b)^2]^{1/2}} \tag{15}$$

The function $f_b = r_b - r_b(z, \phi) = 0$ describes the body surface

[Eq. (3)]. Once $\Delta\theta$ is determined the velocity vector is rotated back into the surface tangent plane by imposing a simple compression or expansion wave.

If $\Delta\theta$ is positive, then an expansion is necessary for the rotation of $\bar{\mathbf{q}}_{1,j}^{n+1}$ and if $\Delta\theta$ is negative a compression wave is required. The corrected value of the static pressure is found from the integral relation[12] for the Prandtl-Meyer turning angle $\nu(p; H_t, s)$ which depends on pressure and has the total enthalpy and entropy as parameters. The corrected value of pressure is found by solving

$$\nu(p_{1,j}^{n+1}; H_t, s) = \nu(\bar{p}_{1,j}^{n+1}; H_t, s) + \Delta\theta \tag{16}$$

for the pressure $p_{1,j}^{n+1}$. In this equation $\Delta\theta$ is given by Eq. (14). If $\Delta\theta$ is sufficiently small, Eq. (16) can be inverted and solved analytically for $p_{1,j}^{n+1}$ only in the case of a perfect gas.[2]

For a real gas, Eq. (16) can be inverted by the use of a table lookup method. The isentropic flow assumption underlying Abbett's boundary condition procedure requires that the table be generated only once at the very beginning of a flowfield calculation when the entropy on the body stream surface is known. The table elements are pressure and Prandtl-Meyer turning angle ν. The procedure for generating the table is described by Hayes and Probstein.[12]

The pressure $p_{1,j}^{n+1}$ appearing in Eq. (16) is determined by first finding $\nu(\bar{p}_{1,j}^{n+1}; H_t, s)$ from the table with the predicted pressure $\bar{p}_{1,j}^{n+1}$ as the argument. The angle $\Delta\theta$ given by Eq. (14) is then added to the result and the desired value for the corrected pressure $p_{1,j}^{n+1}$ is then found from the same table with $\nu(\bar{p}_{1,j}^{n+1}; H_t, s) + \Delta\theta$ as the argument. The remaining flow variables $\rho_{1,j}^{n+1}$, $u_{1,j}^{n+1}$, $v_{1,j}^{n+1}$, and $w_{1,j}^{n+1}$ are then obtained in the same fashion as described in Ref. 2.

The outer boundary of the computational plane is the peripheral shock wave which completely encompasses the disturbed flow region. In this paper a procedure is used whereby the peripheral shock wave (i.e., the shock for which freestream conditions are maintained on the upstream side) is treated as a discontinuity. The Rankine-Hugoniot relations are satisfied exactly across this discontinuity.

There are many ways of incorporating a sharp-shock calculation in a numerical algorithm, including method of characteristics and simpler methods such as those of Barnwell, [13] Kentzer,[14] and Thomas et al.[15] Thomas' scheme is used here since it is relatively simple to implement and, furthermore, comparisons with other methods,[16] including a full method of characteristics, have shown it to yield sufficiently accurate results for our purpose.

The pressure downstream of the shock wave is the basic variable on which all other shock-wave variables depend. Its estimated value $p_{N_{\xi},j}^{(1)}$, $2 \leqq j \leqq N_\eta$ at $(n+1)\Delta z$, is first found by the predictor step Eq. (11a). Since all other variables associated with the shock wave can be expressed as functions of pressure through the Rankine-Hugoniot equations, their values can then be found. The pressure $p_{N_{\xi},j}^{n+1}$ is then recomputed by the corrector, Eq. (11b), and the dependent flow variables are adjusted accordingly.

In the following discussion the required equations will be described. Two quantities will appear in these equations which are inherently dependent on equations of state. These quantities are the upstream component of velocity normal to the shock surface, $\tilde{u}_1$ and the downstream density ρ_2 which are symbolized by

$$\tilde{u}_1 = \tilde{u}_1(p_2; p_1, \rho_1) \tag{17}$$

$$\rho_2 = \rho_2(p_2; p_1, \rho_1) \tag{18}$$

Here we adhere to the conventional practice of denoting the quantities up and downstream of the shock wave discontinuity by the subscripts 1 and 2, respectively, and of separating arguments which are variables from those which are parameters by a semicolon. Note that the upstream components of pressure and density are the freestream values. The procedure used to evaluate Eqs. (17) and (18), which depends on whether a real or perfect gas is considered, is covered later. We assume that such relations exist for the present.

The vector components of velocity normal and tangential to the shock wave are given by

$$\tilde{\mathbf{u}}_1 = -(\mathbf{q}_\infty \cdot \mathbf{n}_s)\mathbf{n}_s \tag{19}$$

$$\tilde{\mathbf{v}}_1 = \mathbf{q}_\infty - \tilde{\mathbf{u}}_1 \tag{20}$$

where $\mathbf{n}_s$ denotes the outward unit normal to the shock surface. The formula for the shock surface normal is identical with that for the body surface normal, Eq. (15), except that the subscript b is replaced by the subscript s.

The magnitude of the normal velocity component, $\tilde{\mathbf{u}}_1$, can be found as a function of shock surface derivatives by the use of Eq. (19). The resulting expression is then inverted to find the following representation for the derivative r_{s_z}:

$$r_{s_z} = u_\infty \Omega + \tilde{u}_1 \{\Omega^2 + [1 + (r_{s_\phi}/r_s)^2]/(u_\infty{}^2 - \tilde{u}_1{}^2)\}^{1/2} \tag{21}$$

where

$$\Omega = [v_\infty - w_\infty (r_{s_\phi}/r_s)]/(u_\infty{}^2 - \tilde{u}_1{}^2)$$

The downstream velocity $\mathbf{q}_2$ is given by either

$$\mathbf{q}_2 = u_{N_\xi}\mathbf{i}_z + v_{N_\xi}\mathbf{i}_r + w_{N_\xi}\mathbf{i}_\phi \quad \text{or} \quad \mathbf{q}_2 = \tilde{\mathbf{u}}_2 + \tilde{\mathbf{v}}_2 \tag{22}$$

The tangential component $\tilde{\mathbf{v}}_2$ is conserved across the shock wave and, hence, its value is the same as $\tilde{\mathbf{v}}_1$. This variable is eliminated from Eq. (22) by the use of Eq. (20) and, in addition, mass conservation across the shock wave is introduced in the form $\tilde{\mathbf{u}}_2 = \tilde{\mathbf{u}}_1 \rho_1/\rho_2$ to eliminate $\tilde{\mathbf{u}}_2$. The result is

$$\mathbf{q}_2 = \mathbf{q}_\infty - r_{s_z} a \mathbf{i}_z + a \mathbf{i}_r - (r_{s_\phi}/r_s) a \mathbf{i}_\phi \tag{23}$$

where

$$a = |\tilde{u}_1|(1 - \rho_1/\rho_2)/[r_{s_z}{}^2 + 1 + (r_{s_\phi}/r_s)^2]^{1/2}$$

These equations are applied in the shock-wave boundary condition scheme in the following manner. The shock-wave radial distance $r_{s_j}^{(1)}$ is evaluated first by use of the Euler predictor

$$r_{s_j}^{(1)} = r_{s_j}^{n} + \Delta z r_{s_{z_j}}^{n} \qquad 2 \leqq j \leqq N_\eta \tag{24}$$

where $r_{s_{z_j}}$ is obtained from Eq. (21). The derivative $r_{s_{\phi_j}}^{(1)}$ is then obtained by the second-order central difference formula

$$r_{s_{\phi_j}}^{(1)} = (r_{s_{j+1}}^{(1)} - r_{s_{j-1}}^{(1)})/2\Delta\phi \qquad 2 \leqq j \leqq N_\eta \tag{25}$$

With the value $\tilde{u}_{1_j}^{(1)} = \tilde{u}_1(p_{N_\xi,j}^{(1)}; p_1, \rho_1)$ obtained by using $p_{N_\xi,j}^{(1)}$ from the predictor [Eq. (11a)], Eq. (21) is evaluated to obtain $r_{s_{z_j}}^{(1)}$. With the addition of $\rho_{2_j}^{(1)} = \rho_2(p_{N_\xi,j}^{(1)}; p_1, \rho_1)$ evaluated from Eq. (18) and, with Eq. (23), $u_{N_\xi,j}^{(1)}$, $v_{N_\xi,j}^{(1)}$, and $w_{N_\xi,j}^{(1)}$ can be found. The predictor step is then completed. The corrector step differs from the predictor step only in that the modified Euler corrector

$$r_{s_j}^{n+1} = r_{s_j}^{n} + (\Delta z/2)(r_{s_{z_j}}^{n} + r_{s_{z_j}}^{(1)}) \tag{26}$$

is used in place of Eq. (24) and $p_{N_\xi,j}^{n+1}$ is obtained from Eq. (11b).

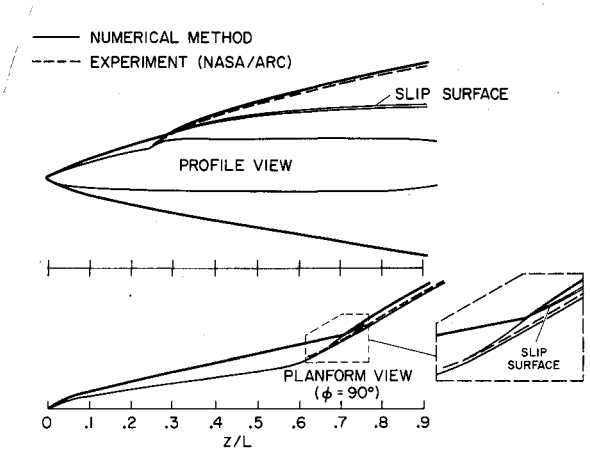

Fig. 4 Shock locations for pointed configuration; $M = 7.4$, $\alpha = 0°$.

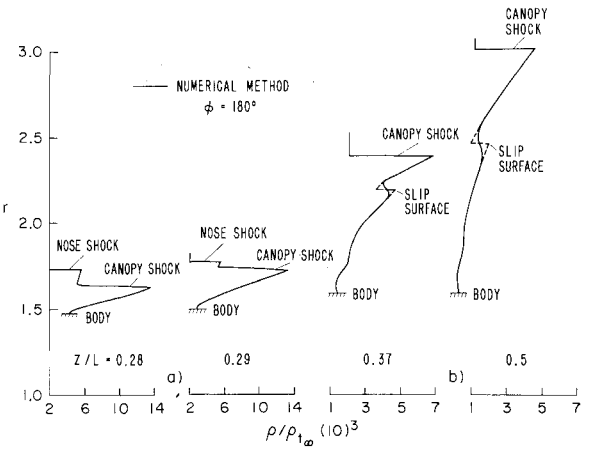

Fig. 5 Intersection of canopy shock with nose shock; $M = 7.4$, $\alpha = 0°$. a) Propagation of canopy shock through shock layer; b) propagation of contact surface through shock layer.

Formulas for Eqs. (17) and (18) in the case of a perfect gas are conventional relations obtained from the Rankine-Hugoniot equations.[15-18] For an equilibrium flow, equivalent analytical representations are not available. A table lookup scheme, however, can also be adapated here as in the surface-boundary condition scheme. At the beginning of the flowfield calculation after p_1 and ρ_1 are specified, a pair of tables is generated that contains the upstream normal velocity $\tilde{u}_1$ and the downstream density ρ_2 as elements with the pressure p_2 as the argument. The table lookup procedure can then simultaneously return values $\tilde{u}_1$ and ρ_2 for a given pressure p_2. The procedure used to generate the table is similar to the method described by Vincenti and Kruger (Ref. 18, p. 179) in their discussion on steady shock waves.

The boundary conditions at the planes of symmetry are applied in the conventional manner whereby the fringe points (see Fig. 2b) are filled with data reflected across the planes of symmetry, e.g., $p_{i,1} = p_{i,3}$, $w_{i,1} = -w_{i,3}$, etc.

VI. Numerical Results

All computations for the results presented here were performed on either an IBM 360/67 or 370/195 linked with a cathode-ray display tube (CRT). The calculations are readily controlled and efficiently performed when using the CRT with its interactive capability.

Three sequences of results are presented which demonstrate the capabilities and limitations of the present numerical procedure for solving multishocked flowfields. The examples apply to flowfields surrounding space-shuttle orbiter vehicles. One set of results compares real and perfect gas effects at a Mach number of 26.26 and angle of attack of 15.3°, while the remaining results are for a perfect gas at Mach 7.4 and either 0° or 15.3° angle of attack.

To test the ability of the numerical procedure to describe the multishocked flowfield surrounding a shuttlelike configuration, a body was designed which used segments 2–3 (bottom ellipse) and 6–7 (top ellipse). The longitudinal variation of the required geometrical parameters was obtained from drawings of a now obsolete delta-wing shuttle orbiter. The resulting analytical configuration modeled the exact shape in both the planform and profile views but crudely approximated the body cross section in the wing region. The actual models that were tested in the wind tunnels also varied somewhat from the blueprint designs due to such replication problems as mold shrinkage. Such effects cause additional discrepancy between the analytical and experimental body shapes. The flow conditions for this test were Mach 7.4 and 0° angle of attack. These particular conditions are of interest computationally because available experimental shadowgraphs[20] show two shock-shock intersection regions; one when the canopy shock intersects the bow shock and the other when the wing leading-edge shock intersects the bow shock. In order to eliminate any difficulties associated with the thinning entropy layer due to a blunt nose, a 23.07° pointed cone was used to simulate the nose of the vehicle for this test case. The grid size in the radial direction consisted of 18 points initially and was increased to 31 points just before the canopy was encountered. The number of meridional planes was held fixed at 19 for the entire calculation, however, the clustering parameter κ of Eq. (4) was varied discretely from a value of 1.0 initially to a value of 0.13 for the last few steps. Its variation was based on the surface pressure distribution in the region of the wing's leading edge as observed on the CRT. This calculation, which consisted of approximately 700 streamwise integration steps and covered over 90% of the body, required about 36 min on an IBM 360/67.

The shock locations in both the planform and profile views are compared with the experimental shadowgraphs made by Cleary[20] in Fig. 4. When the results obtained by the numerical solution coincide with those of the experiment, only the numerical solution is shown. The agreement is excellent even though the actual nose was approximated by a pointed cone. The canopy shock location disagrees somewhat from that of the experiment. This can be attributed to the fact that the simulated canopy was a little steeper than the actual canopy. When the canopy shock intersected the bow shock, the shock fitting procedure automatically started treating the canopy (outermost) shock as a discontinuity and encountered no difficulty in making the transition. The slip surface or inviscid shear layer that results when two shocks of the same family intersect was observed as a rapid change in a small region of the radial density distribution and is also shown in Fig. 4. It agrees identically with that seen in the shadowgraph. In the planform view the intersection of the nose and wing leading-edge shock is shown along with coalesced shock and slip surface. Also shown is the experimental wing shock. There is disagreement between the locations of the numerical and experimental shocks, since in the numerical calculation the actual wing is crudely approximated on the upper surface by a much thicker wing which results in a larger standoff distance.

Plots of the radial density distribution in the leeward ($\phi = 180°$) plane of symmetry before and after the nose shock-canopy shock intersection are shown in Figs. 5a and 5b. Figure 5a shows the propagation of the canopy shock through the nose shock layer while Fig. 5b shows the propagation of the slip surface through the canopy shock layer.

Cross sections of the body and shock shape are shown in Fig. 6 at a $z/L = 0.87$. The distribution of the meridional points used in the calculation are shown along the peripheral shock to

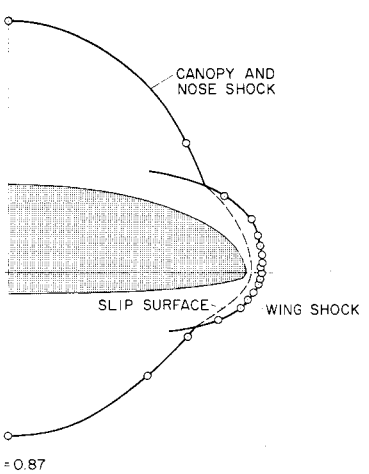

Fig. 6 Body and shock cross sections for pointed configuration; $M = 7.4$, $\alpha = 0°$.

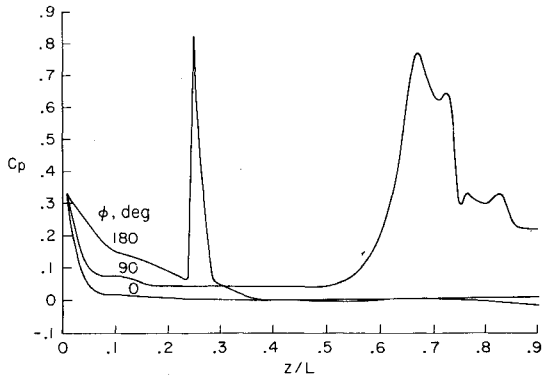

Fig. 7 Longitudinal surface pressure distributions for the 0°, 90°, and 180° meridians; $M = 7.4$, $\alpha = 0°$.

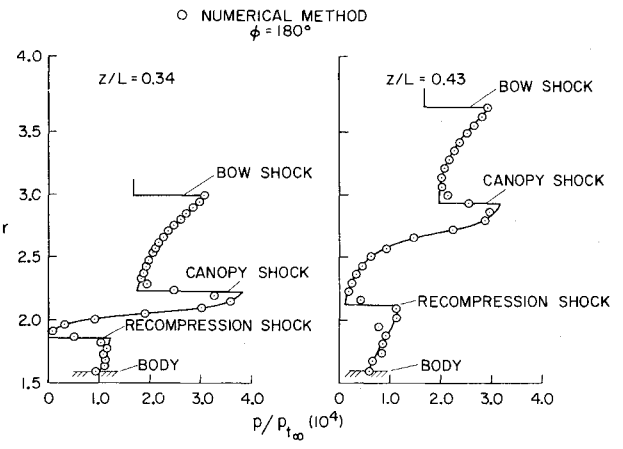

Fig. 9 Propagation of canopy and recompression shocks through shock layer in leeward plane of symmetry; $M = 7.4$, $\alpha = 15.3°$.

provide an idea of the degree of clustering that was used. Also shown in this figure is the approximate location of the slip surface which stretches from the two shock intersection points.

The longitudinal surface pressure distribution in the 0°, 90°, and 180° meridians is shown in Fig. 7. The rapid rise and fall in pressure at a $z/L = 0.25$ in the 180° plane is caused by the canopy. The rapid rise in pressure in the 90° plane at a $z/L = 0.55$ is due to the wing starting to compress the flow. The pressure in the $\phi = 0°$ plane decreases as the boattail of the shuttle on the lower surface comes into effect. The boattail is generated by a decreasing semiminor axis of the bottom ellipse which results in an increasing ellipticity ratio. This caused the gradients of the flow variables near the leading edge to become unwieldy and eventually caused termination of the calculations. The results obtained for this case compared quite accurately with those obtained using the shock capturing technique[2] as well as with the method of characteristics.[8,22]

Some interesting results are obtained when a similar configuration is tested; this time with a blunt nose and at angle of attack. The flow conditions are a Mach number of 7.4 and angle of attack of 15.3°. The radial distribution of points was varied from 21 initially to 31 finally. The number of meridional planes was kept constant at 19 while the clustering parameter κ was changed when necessary.

The planform and profile shock shapes are shown in Fig. 8 and compared with the experimental shadowgraphs and with the method of characteristics.[8] The windward portion of the shock agrees quite well with experiment, and the slight variance at its latter stations can be attributed to the disagreement between the numerical and experimental body shapes on the forward portion of the lower surface. On the leeward side the canopy shock was captured, but its location disagreed somewhat from that of the experiment, again due to the differences in bodies. Because of the overexpansion of the flow around the canopy, a recompression shock is formed, and is also shown in Fig. 8. It is weaker than the canopy shock and was not observed in this shadowgraph. However, it has been observed in other experiments.[21] The shock which was generated by the wing leading edge is shown in the planform view ($\phi = 90°$) of Fig. 8. Its location in this view agrees well with the experiment, since the bottom ellipse closely approximates the lower surface of the shuttle and also controls the shock standoff distance at the leading edge.

Figure 9 shows the pressure distribution in the radial direction for the leeward plane of symmetry at two longitudinal stations, in which both the canopy and recompression shocks are recognizable. Both shocks are captured within two or three mesh intervals.

Radial pressure and density plots through the merged entropy layers as well as the wing leading-edge shocks are shown in Fig. 10. The wing leading-edge shock in this plane is spread over four mesh intervals. Although good definition of the entropy layers is lost, their presence posed no difficulties until their thickness became less than one mesh interval, at which time oscillations began to appear.

Cross sections of the body and shock at a z/L of 0.67 are

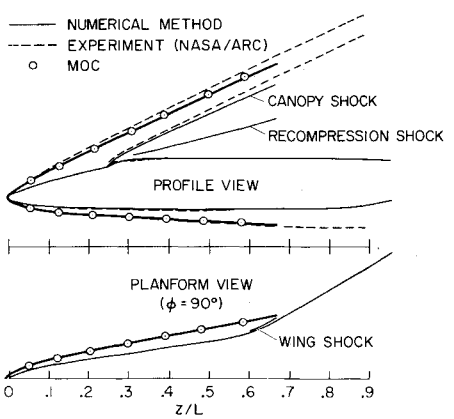

Fig. 8 Shock locations for blunt nosed configuration; $M = 7.4$, $\alpha = 15.3°$.

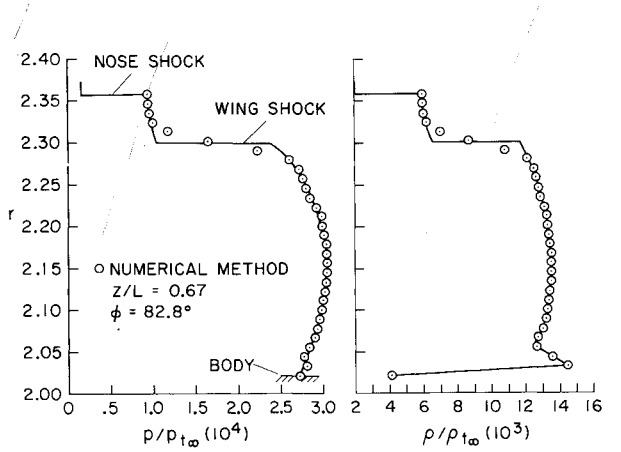

Fig. 10 Radial pressure and density distribution through entropy layer and wing leading edge shock; $M = 7.4$, $\alpha = 15.3°$.

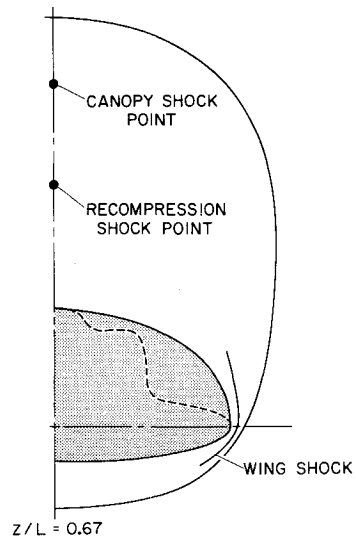

Fig. 11 Body and shock cross sections for blunt nose configuration; $M = 7.4$, $\alpha = 15.3°$.

shown in Fig. 11. The wing leading shock wraps itself around the body and becomes infinitesimal in strength at the planes of symmetry. Only the points found by the automatic shock seeking routine are plotted for the wing shock. The distribution of meridional points on the lee side becomes sparse when κ is small and, therefore, resolution of the leeward canopy and recompression shocks is impaired. However, these shocks are readily distinguishable in the lee plane of symmetry data and their location in this plane is shown by the points in Fig. 11.

The longitudinal surface-pressure distribution for three meridians is shown in Fig. 12 and compared with experimental data obtained from the NASA/ARC 3½ ft hypersonic wind tunnel. As the integration proceeds downstream, the pressure in the 85° plane continually rises causing a corresponding decrease in the u component of velocity, to the extent that u approaches its local sonic value. This eventually causes termination of the calculations since the equations are then no longer hyperbolic. These near sonic velocities occur only within the entropy layer, and the velocities are well above sonic outside of this layer.

In order to demonstrate the method's capability to calculate equilibrium air flow, starting conditions were chosen representative of a point on the orbiter's trajectory; namely, an altitude of 76 km, a velocity of 7.3 km/sec ($M = 26.26$) and an angle of attack of 15.3°. Freestream conditions like these are difficult to simulate in existing wind-tunnel facilities. The results of

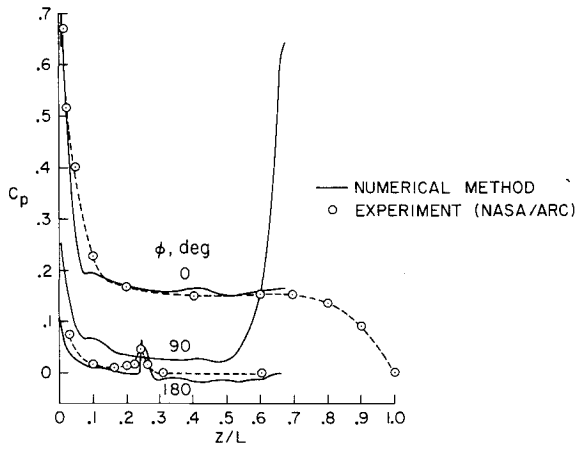

Fig. 12 Longitudinal surface pressure distribution for the 0°, 90°, and 180° meridians; $M = 7.4$, $\alpha = 15.3°$.

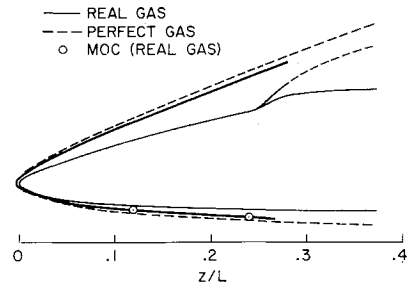

Fig. 13 Comparison of shock location for blunt nose configuration; $M = 26.26$, $\alpha = 15.3°$, alt = 76 km.

calculations for the forward fuselage of a shuttle-like configuration are shown in Fig. 13 in which the shock shapes for both perfect and real gases are compared. Also shown are results from a real gas method of characteristics calculation[6] which are given by the circles. Agreement between both numerical methods is excellent.

Also shown in Fig. 13 is a small segment of the secondary shock originating from the front of the canopy. Here, no differences between the perfect and real gas solutions are observed.

References

[1] Morretti, G., Grossman, B., and Marconi, F., Jr., "A Complete Numerical Technique for the Calculation of Three Dimensional Inviscid Supersonic Flows," AIAA Paper 72-192, San Diego, Calif., 1972.

[2] Kutler, P., Lomax, H., and Warming, R. F., "Computation of Space Shuttle Flow Fields Using Noncentered Finite-Difference Schemes," AIAA Paper 72-193, San Diego, Calif., 1972.

[3] MacCormack, R. W., "The Effect of Viscosity in Hypervelocity Impact Cratering," AIAA Paper 69-354, Cincinnati, Ohio, 1969.

[4] Woods, B. A., "The Supersonic Flow Past an Elliptic Cone," *The Aeronautical Quarterly*, Vol. 20, 1969, p. 382.

[5] Schiff, L. B., "Computation of Supersonic Flow Fields About Bodies in Coning Motion Using a Shock-Capturing Finite-Difference Technique," AIAA Paper 72-27, San Diego, Calif., 1972.

[6] Kutler, P., Rakich, J. V., and Mateer, G. G., "Application of Shock Capturing and Characteristics Methods to Shuttle Flow Fields," TM X-2506, Vol. 1, 1972, NASA, p. 65.

[7] Dekker, T. J., *Constructive Aspects of the Fundamental Theorem of Algebra*, edited by B. Dejon and P. Henrici, Wiley, New York, 1969, p. 37.

[8] Rakich, J. V. and Kutler, P., "Comparison of Characteristics and Shock Capturing Methods with Application to the Space Shuttle Vehicle," AIAA Paper 72-191, San Diego, Calif., 1972.

[9] Chu, C. W. and Powers, S. A., "Determination of Space Shuttle Flow Field by the Three-Dimensional Method of Characteristics," TM X-2508, 1972, NASA.

[10] Kutler, P., "Application of Selected Finite Difference Techniques to the Solution of Conical Flow Problems," Ph.D. thesis, 1969, Dept. of Aerospace Engineering, Iowa State Univ., Ames, Iowa.

[11] Abbett, M. J., "Boundary Condition Computational Procedures for Inviscid Supersonic Steady Flow Field Calculations," Final Rept. 71-41, 1971, Aerotherm Corp., Mt. View, Calif.

[12] Hayes, W. D. and Probstein, R. F., *Hypersonic Flow Theory*, 2nd ed., Academic Press, New York, 1966, p. 485.

[13] Barnwell, R. W., "A Time-Dependent Method for Calculating Supersonic Angle-of-Attack Flow About Axisymmetric Blunt Bodies with Sharp Shoulders and Smooth Nonaxisymmetric Blunt Bodies," TN D-6283, 1971, NASA.

[14] Kentzer, C. P., "Discretization of Boundary Conditions on Moving Discontinuities," *Proceedings of the 2nd International Conference on Numerical Methods in Fluid Dynamics, Lecture Notes in Physics*, Vol. 8, Springer-Verlag, Berlin, 1971.

[15] Thomas, P. D., Vinokur, M., Bastianon, R., and Conti, R. J., "Numerical Solution for the Three-Dimensional Inviscid Supersonic Flow," *AIAA Journal*, Vol. 10, No. 7, July 1972, pp. 887–894.

[16] Abbett, M. J., "Sharp Shock Computational Procedures for

Inviscid, Supersonic, Steady Flow Field Calculations," Rept. 72-50, 1972, Aerotherm Corp., Mt. View, Calif.

[17] Ames Research Staff, "Equations, Tables, and Charts for Compressible Flow," Rept. 1135, 1953, NACA.

[18] Vincenti, W. G. and Kruger, C. H., Jr., *Introduction to Physical Gas Dynamics*, Wiley, New York, 1965.

[19] Lomax, H. and Inouye, M., "Numerical Analysis of Flow Properties About Blunt Bodies Moving at Supersonic Speeds in an Equilibrium Gas," TR R-204, 1964, NASA.

[20] Cleary, J. W., "Hypersonic Shock-Wave Phenomena of a Delta-Wing Space-Shuttle Orbiter," TM X-62,076, 1971, NASA.

[21] Cleary, J. W., "Subsonic, Transonic, and Supersonic Stability and Control Characteristics of a Delta Wing Orbiter," TM X-62,066, 1970, NASA.

[22] Rakich, J. V., "Three-Dimensional Flow Calculations by the Method of Characteristics," *AIAA Journal*, Vol. 5, No. 10, Oct. 1967, pp. 1906–1908.

MAY 1973 AIAA JOURNAL VOL. 11, NO. 5

Nitric Oxide Formation in Gas Turbine Combustors

R. KOLLRACK* AND L. D. ACETO†
Pratt & Whitney Aircraft Division, United Aircraft Corporation, East Hartford, Conn.

The net nitric oxide (NO) formation is influenced not only by the thermodynamic (equilibrium) aspects of the combustion process but also by the detailed intermediate hydrocarbon reaction kinetics. An analytical study was made to obtain a representative combustion reaction mechanism for gas turbines. This mechanism was used to determine the OH, O, H, and N radical levels occurring during the combustion process. Simultaneously, the resulting NO formation was established. OH and O radical concentrations exceeding the equilibrium concentrations by up to two orders of magnitude were obtained with durations controlled by the combustion of raw fuel. This analysis, which covers premixed combustion, was extended to demonstrate the influences of droplet vaporization and staged fuel addition. The NO levels resulting from liquid fuel combustion were found to be up to two orders of magnitude larger than the NO levels of premixed combustion.

1. Introduction

THE main use of gas turbines is to power commercial or military aircraft. Averaging over the total nation, only a small portion of the ground level air pollution has been estimated as caused by gas turbines.[1] However, in the vicinity of airports, aircraft taxiing, taking off, or landing are major producers of various air pollutants.

As a result of continuous combustion at relatively high temperatures, aircraft gas turbine engines form NO_x compounds at peak rates under full-load (takeoff) conditions. Nitric oxide (NO) is the primary nitrogen oxygen compound produced in any airbreathing engine.[1] The formation of NO is extremely temperature dependent and occurs mainly during the period of highest temperature, i.e., within the primary combustion zone and early in the secondary zone, where the additional air allows for combustion to approach stoichiometric conditions but before the quenching effect, due to further dilution with air, becomes dominant. The maximum temperature reached is very near the equilibrium value. At this point, most combustion products are believed to approach their equilibrium concentrations. This steady-state condition of equilibrium levels of O and N atoms and OH radicals allows the calculation of the NO formation rate from the relatively well-known rate constants of the three most important NO forming reactions.[2,15] However, measurements of gas turbine burners have shown NO levels greater than those predicted by the steady-state analytical method.

Fenimore et al.[3] introduced reactions between carbon and nitrogen to explain these high NO formation rates. No reaction rate data were given. It seems to be questionable whether these reactions could be fast enough to produce the NO levels required.

An adequate explanation can be seen when details of the combustion phenomena are exposed. The onset of active combustion creates as byproducts concentrations of O and OH radicals in excess of their equilibrium levels. Subsequently, these radical overshoots accelerate the rates of the conventional NO-producing reactions above the NO formation rates of the aforementioned steady-state condition.

The present study is an extension of the results reported by Roberts et al.[2] covering these overshoots for premixed and liquid fuel combustion. The analysis was done with a Pratt & Whitney Aircraft developed program which numerically solves simultaneously the chemical kinetic, thermodynamic, and gas-dynamic equations.

2. Combustion Model

All the investigations reported herein have assumed a constant-area combustor model. Premixed combustion starts with a mixture of vaporized fuel and air at a temperature of 1000°K or more. It should be noted that self-ignition of commercial jet fuel does not occur below this temperature and, in effect, the ignition and recirculation patterns of combustors are such to maintain the incoming mixture at an effective temperature of 1000°K or higher.

The fuel and air remain approximately at this temperature for a period during which the endothermic breakdown reactions of the original fuel molecule and the subsequent highly exothermic reactions of the fuel intermediates are nominally balanced. This ignition delay time is followed by an abrupt temperature rise, where the exothermic reactions progressively take over. Thereafter, a gradual approach to the equilibrium temperature and

Received October 12, 1972; revision received January 15, 1972.
Index categories: Combustion in Gases; Combustion in Heterogeneous Media; Reactive Flows.

* Associate Research Scientist.
† Research Engineer. Member AIAA.